

Apparent Places with an Ellipsoidal Geometry of Refraction in the Earth's Atmosphere

Richard J. Mathar*

Leiden Observatory, Leiden University, P.O. Box 9513, 2300 RA Leiden, The Netherlands

(Dated: March 12, 2019)

The displacement of star images by atmospheric refraction observed by an Earth-bound telescope is dominated by a familiar term proportional to the tangent of the zenith angle and proportional to the refractivity at the ground.

The manuscript focuses on the torsion of the ray path through the atmosphere in a model of ellipsoidal atmospheric layers above the Earth surface, induced by the two slightly different principal curvatures along N–S and E–W pointing directions, depending on the geodetic latitude of the telescope site. This symmetry breaking effects apparent places in the sub-milliarcsecond range at optical and infrared wavelengths.

PACS numbers: 95.75.Mn, 95.10.Jk

Keywords: Atmospheric Refraction, Astronomy, Apparent Place, Prolate Ellipsoid

I. RAY PATHS FROM SNELL'S LAW

Tracing of rays of stellar light through the Earth atmosphere is a repeated application of Snell's law of refraction, as the refractive index n increases from $n - 1 = 0$ high above the atmosphere to $n - 1$ of the order of 2×10^{-4} —perhaps 3×10^{-4} at sea level—at the telescope site. The angle between their direction τ_0 at arrival at the telescope and the topocentric zenith is smaller than in a calculation with vacuum replacing the atmosphere [1, 3, 5, 16, 17]; the atmosphere is a gradient lens [7, 10, 11]. The ray path is curved. Snell's law of the relation between refractive index n and incidence angle ψ relative to the normal to the layered atmosphere is

$$n \sin \psi = \text{const.} \quad (1)$$

The first differential of this equation is

$$\Delta n \sin \psi + n \cos \psi \Delta \psi = 0, \quad (2)$$

or upon division through $\cos \psi$

$$\Delta n \tan \psi = -n \Delta \psi, \quad (3)$$

which explains in conjunction with $n - 1 \ll 1$ why the difference between true and apparent positions, the accumulation of all $\Delta \psi$, basically turns out proportional to the tangent of the zenith angle.

The continuum version is equivalent to solving the differential equation which couples the gradient of the refractive index to the ray's curvature [2, chap. 3.2]

$$\frac{d}{ds} \left(n \frac{d\mathbf{r}}{ds} \right) = \nabla n \quad (4)$$

for the path \mathbf{r} as a function of path length s . This can be transformed to general curvilinear coordinates [4], and

has been made explicit for the Earth ellipsoid by Yatsenko [19]. The present work demonstrates that the asphericity changes apparent places by less than one milliarcsecond, such that a simple finite-element computation suffices for all but some ambitious astrometry projects.

II. NUMERICAL SIMULATION

A. Oblate Ellipsoid Coordinates

The Cartesian coordinates of a position \mathbf{r} are related to the geodetic latitude ϕ , geodetic longitude λ and height h above the ellipsoid as [8]

$$\mathbf{r} = \begin{pmatrix} (N + h) \cos \phi \cos \lambda \\ (N + h) \cos \phi \sin \lambda \\ [N(1 - e^2) + h] \sin \phi \end{pmatrix}, \quad (5)$$

where

$$N(\phi) \equiv \frac{\rho_e}{\sqrt{1 - e^2 \sin^2 \phi}} \quad (6)$$

is the distance to the Earth axis along the surface normal. $\rho_e \approx 6378$ km and $e \approx 0.0818$ are equatorial radius and eccentricity [13].

B. Refractive Index of Altitude

The simulation has been performed with an exponential model of the air susceptibility $\chi(h)$ as a function of altitude h , which changes in discrete steps at altitudes h_i such that the kinks $n(h_{i+1}) - n(h_i)$ are approximately equal across each interface:

$$n(h) = \sqrt{1 + \chi_i}; \quad h_i \leq h \leq h_{i+1}. \quad (7)$$

This is achieved by defining a set of heights a_i as a logarithmic function of index i , using each second to specify

*URL: <http://www.strw.leidenuniv.nl/~mathar>; Electronic address: mathar@strw.leidenuniv.nl

interface locations h_i , and using the complementary set of interlaced heights to specify the χ_i :

$$a_i = K \log\left(\frac{i_\infty}{i_\infty - i}\right), \quad 0 \leq i < i_\infty; \quad (8)$$

$$h_i = a_{2i-1}; \quad 1 \leq i \leq i_\infty/2; \quad (9)$$

$$\chi_i = \chi_0 e^{-a_{2i}/K}, \quad 0 \leq i < i_\infty/2; \chi_{i_\infty/2} = 0. \quad (10)$$

The scale height was set to $K = 9.6$ km and the ground layer value to $\chi_0 = 4 \times 10^{-4}$. The results are practically stable once the number of layers, that is $i_\infty/2$, is set to values of order 10 or 20.

C. Finite Element Segmentation

Rays are traced backwards from the position \mathbf{r}_0 of the telescope to the vacuum above the troposphere. This removes the need to implement some adaptive forward searching techniques for the alternative handling which would trace the ray in its natural direction.

The implementation is much simpler than writing down the associated first order differential equation of the eikonal in the curvilinear coordinates [9].

At each layer interface, a topocentric coordinate system is spanned by the unit vectors \mathbf{e}_ϕ , \mathbf{e}_λ and \mathbf{e}_h [12]

$$\mathbf{e}_\phi \equiv \frac{\partial}{\partial \phi} \mathbf{r}, \quad \mathbf{e}_\lambda \equiv \frac{\partial}{\partial \lambda} \mathbf{r}, \quad \mathbf{e}_h \equiv \frac{\partial}{\partial h} \mathbf{r}. \quad (11)$$

The positions along the straight paths inside the layers are defined as

$$\mathbf{r} = \mathbf{r}_i + t \boldsymbol{\tau}_i \quad (12)$$

via a direction $\boldsymbol{\tau}$ and distance parameter t . Given the altitude h_{i+1} of the next layer as defined by the layer model above, the unknowns t , ϕ_{i+1} and λ_{i+1} which constitute \mathbf{r}_{i+1} are calculated by solving

$$\mathbf{r}_i + t \boldsymbol{\tau}_i = \begin{pmatrix} [N(\phi_{i+1}) + h_{i+1}] \cos \phi_{i+1} \cos \lambda_{i+1} \\ [N(\phi_{i+1}) + h_{i+1}] \cos \phi_{i+1} \sin \lambda_{i+1} \\ [N(\phi_{i+1})(1 - e^2) + h_{i+1}] \sin \phi_{i+1} \end{pmatrix}. \quad (13)$$

This nonlinear system of 3 equations and 3 unknowns is reduced to 2 equations and 2 unknowns by taking the sum of the squares of the first two components, which eliminates λ_{i+1} , and then solved by a Newton method.

Once the h_{i+1} , ϕ_{i+1} and λ_{i+1} are known, a local triad ($\mathbf{e}_\phi, \mathbf{e}_\lambda, \mathbf{e}_h$) is set up at the interface point \mathbf{r}_{i+1} . The direction $\boldsymbol{\tau}_i$ is virtually decomposed as

$$\boldsymbol{\tau}_i = \alpha \mathbf{e}_{\phi,i+1} + \beta \mathbf{e}_{\lambda,i+1} + \gamma \mathbf{e}_{h,i+1} \quad (14)$$

that is, the angle of incidence ψ is computed as the projection

$$\boldsymbol{\tau}_i \cdot \mathbf{e}_{h,i+1} = \cos \psi |\boldsymbol{\tau}_i| |\mathbf{e}_{h,i+1}| = \gamma |\mathbf{e}_{h,i+1}|^2. \quad (15)$$

Snell's law fixes the exit angle χ

$$n_{i+1} \sin \chi = n_i \sin \psi, \quad (16)$$

and the new direction $\boldsymbol{\tau}_{i+1}$ is constructed by switching in a new projection γ' for the old γ as

$$\gamma \tan \psi = \gamma' \tan \chi; \quad (17)$$

$$\boldsymbol{\tau}_{i+1} = \alpha \mathbf{e}_{\phi,i+1} + \beta \mathbf{e}_{\lambda,i+1} + \gamma' \mathbf{e}_{h,i+1}. \quad (18)$$

The procedure is iterated with the parametrization $\mathbf{r}_{i+1} + t \boldsymbol{\tau}_{i+1}$ for the path inside the next layer. The decomposition (14) is virtual in the sense that α , $\mathbf{e}_{\phi,i+1}$, β and $\mathbf{e}_{\lambda,i+1}$ are not actually computed; the new direction is an update of the old by adding the Cartesian components of $(\gamma' - \gamma) \mathbf{e}_{h,i+1}$ to the Cartesian components of $\boldsymbol{\tau}_i$.

The format (14) defines the apparent zenith angle z_0 and apparent azimuth A_0 in the ground layer

$$\boldsymbol{\tau}_0 \cdot \mathbf{e}_{\phi,0} = \sin z_0 \cos A_0 |\mathbf{e}_{\phi,0}|^2; \quad (19)$$

$$\boldsymbol{\tau}_0 \cdot \mathbf{e}_{\lambda,0} = -\sin z_0 \sin A_0 |\mathbf{e}_{\lambda,0}|^2; \quad (20)$$

$$\boldsymbol{\tau}_0 \cdot \mathbf{e}_{h,0} = \cos z_0 |\mathbf{e}_{h,0}|^2, \quad (21)$$

where the azimuth A is counted North-over-West. The simulation produces the true zenith angle z and true azimuth A by the equivalent projection of $\boldsymbol{\tau}_\infty$, the direction at exit above the troposphere, onto the axes of the topocentric system at the telescope, i.e.,

$$\boldsymbol{\tau}_\infty \cdot \mathbf{e}_{\phi,0} = \sin z \cos A |\mathbf{e}_{\phi,0}|^2; \quad (22)$$

$$\boldsymbol{\tau}_\infty \cdot \mathbf{e}_{\lambda,0} = -\sin z \sin A |\mathbf{e}_{\lambda,0}|^2; \quad (23)$$

$$\boldsymbol{\tau}_\infty \cdot \mathbf{e}_{h,0} = \cos z |\mathbf{e}_{h,0}|^2. \quad (24)$$

III. RESULTS

A. Apparent Azimuth

The difference $z - z_0$ is the familiar change in zenith angle. The non-zero difference $A - A_0$ is a measure of the ray torsion [6], which vanishes in the limit of zero eccentricity. This change of apparent azimuth is illustrated in Fig. 1 for the Earth parameters quoted above. The zenith angle z_0 and azimuth A_0 are coded in circular coordinates at the base of each sub-plot: in the center, z_0 is zero, and it grows outwards in steps of 5° such that the maximum $z_0 = 60^\circ$ is reached at the rim of the graph. The azimuth directions N and W are indicated by arrows.

The presence of torsion such that the rays do not stay in a single plane is a side effect of the two different curvatures along the N-S and E-W directions set up by this atmospheric model (App. A). The curvature is larger for pointing into N-S than for pointing into E-W directions. Larger curvature implies smaller air mass, i.e., smaller angles of incidence relative to the normals of the air layers, and implies smaller optical path length.

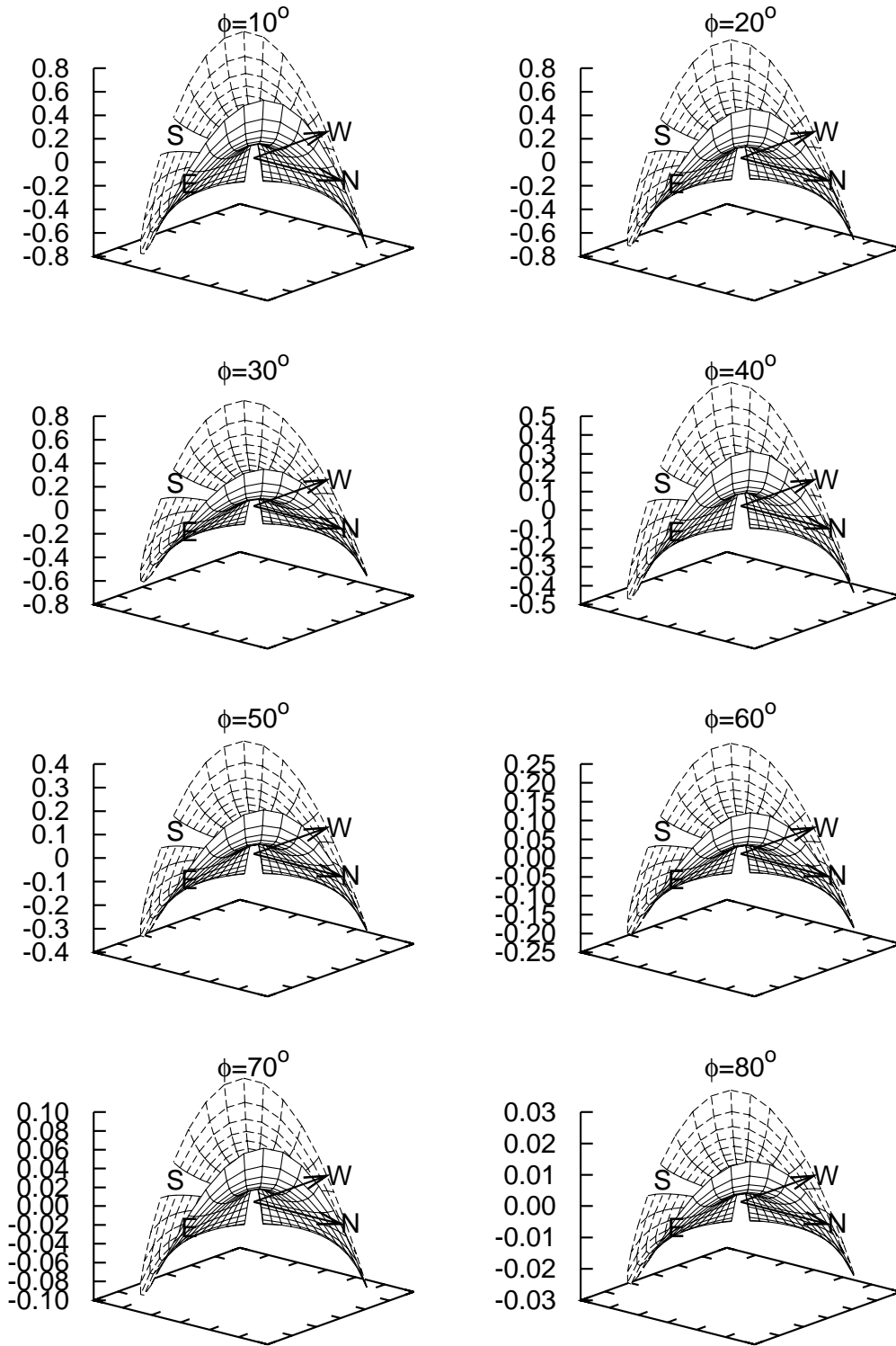


FIG. 1: The difference $A - A_0$ between true and apparent azimuth angles in units of milli-arcseconds for eight different geodetic latitudes ϕ of the telescope as a function of pointing direction (zenith angle zero to 60° growing outwards; azimuth with a deliberate gap in the South direction at $\pm 180^\circ$).

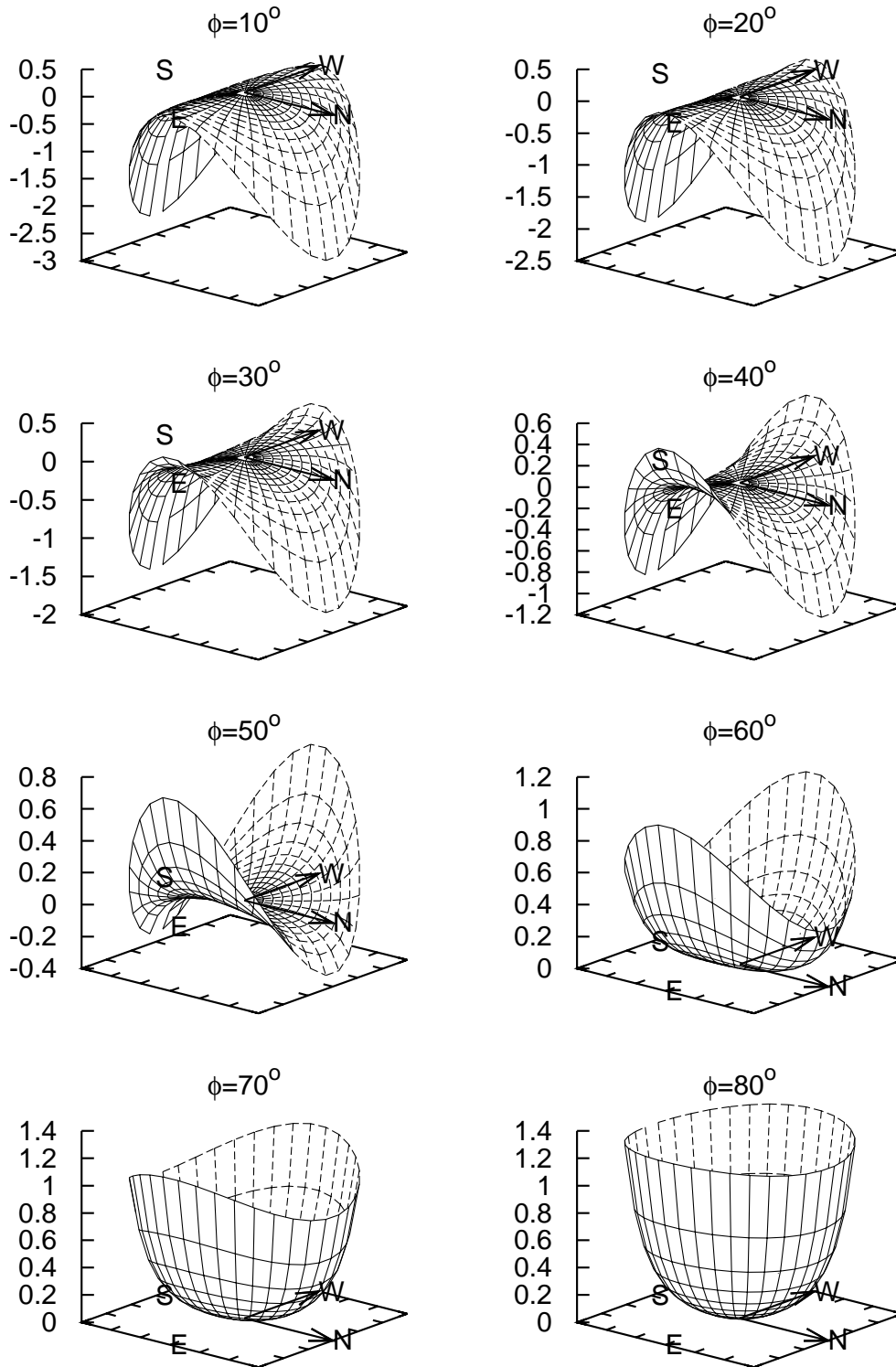


FIG. 2: The difference in star zenith angles obtained with a prolate ellipsoid compared with the computation with a spherical Earth, $(z - z_0)|_e - (z - z_0)|_{e=0}$, in units of milli-arcseconds, for eight geodetic latitudes ϕ plotted as a function of $z_0 \leq 60^\circ$, $-175^\circ \leq A_0 \leq 175^\circ$.

Since Snell's law is a result of the eikonal minimization (Fermat's principle) which lets light select minimum optical path length, the net effect is to steer light closer to the N if it has a northern component, and closer to S if it has southern component. In our convention—azimuths wrapped around such that $|A| \leq 180^\circ$ —, the directions of τ_∞ set azimuths $|A| < A_0$ if $|A_0| < 90^\circ$, and azimuths $|A| > A_0$ if $|A_0| > 90^\circ$. This explains why $A - A_0 < 0$ for NW or SE directions, and why $A - A_0 > 0$ for SW or NE directions, as shown in Fig. 1. The effect vanishes approaching the geodetic poles, $\phi \rightarrow \pm 90^\circ$, because the two curvatures equalize there (Eq. (A10)).

The discontinuity of the plots in Fig. 1 in the centers near $z = 0$ is the standard artifact of polar coordinates. The same reasoning applies which leads to the multiplication of right ascension components of proper motions by the cosine of the declinations.

B. Apparent Zenith

In Fig. 2 we compare the change in zenith angles of τ_∞ as the ellipticity e is switched off to $e = 0$, keeping ρ_e the same. This effect is typically buried under the standard effect up to 60 arcseconds. We see that for telescope sites near the equator, small $|\phi|$, the zenith angles for pointing in E or W direction are the same as calculated for the spherical model, whereas the N or S directions have smaller refractivities. Fig. 2 just tracks the changes in the two principal curvatures (A10) and (A12) and finishes with positive values near $|\phi| \rightarrow 90^\circ$ because the curvature of the prolate model near the poles, radius $\rho_p > \rho_e$, is smaller than the curvature of the spherical model kept at ρ_e .

For $\phi < 54^\circ$ [up to where the line of $\kappa_2(\phi)$ meets the horizontal defined by $\kappa_1(0)$ in Fig. 3], one can find azimuths A for which the difference vanishes as the curvature $\kappa = \sin^2 A \kappa_1 + \cos^2 A \kappa_2$ of Euler's formula equals the equatorial curvature. This explains the saddle shapes in Fig. 2 while $\phi < 54^\circ$. Evidently, the figure would look different if the reference were an Earth sphere with a radius selected from a mean (Gauss) curvature depending on ϕ , for example.

This effect results from any accurate calculation of the standard zenithal apparent places with variable earth radius. The amount of 1 milli-arcsecond for $\phi = 80^\circ$ in Fig. 2 is expected from my earlier calculation [11, Fig. 4], which stated that the effect of replacing the zero curvature model by a model with the standard curvature is 0.5% of $z - z_0$, which accumulates 0.3 arcseconds supposed $z - z_0 \approx 60$ arcseconds. Because the factor $1/\sqrt{1-e^2}$ of (A10) introduces a relative difference of 0.3% between equatorial and polar radii or curvatures, linear extrapolation predicts indeed a change of up to another 1 milli-arcsecond in apparent zenith angle if telescopes are moved between equator and poles [18].

IV. SUMMARY

Ray paths through the atmosphere in the geometric optics approximation change their direction in zenith angle *and* azimuth if the refractive indices in the atmosphere layers are shells modeled with a symmetry of the prolate ellipsoid of the Earth. The change in azimuth direction is less than one milli-arcsecond for pointing less than 60° away from the zenith at typical optical wavelengths, comparable to the diffraction limit of a 170 m telescope, and therefore much smaller than the standard refractivity effect (and others not discussed here [15]) which changes apparent positions on the scale of 60 arcseconds under the same conditions.

APPENDIX A: CURVATURES

The Fundamental Parameters of the first form of the surface of constant altitude h for prolate ellipsoids are [12]

$$\bar{E} = (N + h)^2 \cos^2 \phi; \quad (\text{A1})$$

$$\bar{F} = 0; \quad (\text{A2})$$

$$\bar{G} = (M + h)^2. \quad (\text{A3})$$

The Fundamental Parameters of the second form of the surface are

$$\bar{L} = -(N + h) \cos^2 \phi; \quad (\text{A4})$$

$$\bar{M} = 0; \quad (\text{A5})$$

$$\bar{N} = -(M + h), \quad (\text{A6})$$

where

$$M(\phi) \equiv N(\phi) \frac{1 - e^2}{1 - e^2 \sin^2 \phi}. \quad (\text{A7})$$

The six Fundamental Parameters are adorned with an overbar to set \bar{N} and \bar{M} apart from the distances N and M in (6) and (A7). The two principal curvatures $\kappa_{1,2}(\phi)$ are the roots of the quadratic equation

$$(\bar{E}\bar{G} - \bar{F}^2)\kappa^2 - (\bar{E}\bar{N} - 2\bar{F}\bar{M} + \bar{G}\bar{L})\kappa + (\bar{L}\bar{N} - \bar{M}^2) = 0. \quad (\text{A8})$$

Insertion of the 6 parameters yields

$$(N + h)(M + h)\kappa^2 + (M + N + 2h)\kappa + 1 = 0. \quad (\text{A9})$$

The two solutions $\kappa_1 = -1/(N+h)$ and $\kappa_2 = -1/(M+h)$ are shown in Fig. 3. In particular:

- Above the poles, $\sin \phi = \pm 1$, $N = M$ and

$$\kappa_{1,2}(\phi = \pm\pi/2) = -\frac{1}{\frac{\rho_e}{\sqrt{1-e^2}} + h}, \quad (\text{A10})$$

so the curvatures are derived from the semiminor axis $\rho_p = \rho_e/\sqrt{1-e^2}$ [14].

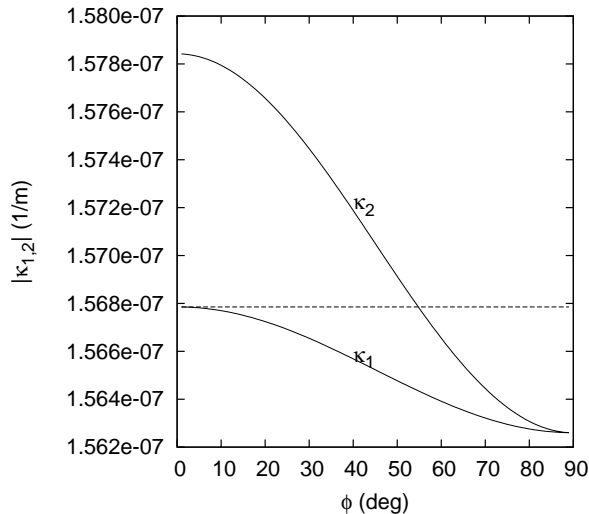


FIG. 3: The principal curvatures from (A9) at $h = 0$ as a function of geodetic latitude.

- Above the equator, $\sin \phi = 0$, $N = \rho_e$, $M = \rho_e(1 - e^2)$ and

$$\kappa_1(\phi = 0) = -\frac{1}{\rho_e + h}, \quad (\text{A11})$$

$$\kappa_2(\phi = 0) = -\frac{1}{\rho_e(1 - e^2) + h}, \quad (\text{A12})$$

which associates with the equatorial radius of curvature ρ_e and the polar radius of curvature $\rho_e(1 - e^2)$ [14].

In the main text we call $|\kappa|$ the curvature; coherent with the standard nomenclature for closed shell surfaces, the negative sign is maintained in this appendix.

-
- [1] Auer, L. H., and E. M. Standish, 2000, *Astron. J.* **119**(5), 2472.
- [2] Born, M., and E. Wolf, 1999, *Principles of Optics* (Cambridge University Press, Cambridge), 7th edition.
- [3] Filippenko, A. V., 1982, *Publ. Astron. Soc. Pac.* **94**, 715.
- [4] Geiger, A., and M. Cocard, 1992, in *Refraction of transatmospheric signals in Geodesy*, edited by J. C. de Munck and T. A. T. Spoelstra (Netherlands Geodetic Commission, The Hague), number 36 in Publications on Geodesy, New Series, pp. 191–195.
- [5] Green, R. M., 1985, *Spherical Astronomy* (Cambridge University Press, Cambridge, London).
- [6] Hubbard, W. B., 1976, *Icarus* **27**(3), 387.
- [7] Hui, L., and S. Seager, 2002, *Astrophys. J.* **572**(1), 540.
- [8] Jones, G. C., 2004, *J. Geod.* **76**(8), 437.
- [9] Kravtsov, Y. A., and Y. I. Orlov, 1990, *Geometrical Optics of Inhomogeneous Media*, number 6 in Springer Series on Wave Phenomena (Springer, Berlin), ISBN 3540519440.
- [10] Marchand, E. W., 1973 (Elsevier, Amsterdam), volume 11 of *Prog. Opt.*, pp. 305–337.
- [11] Mathar, R. J., 2005, *Baltic Astronomy* **14**(2), 277.
- [12] Mathar, R. J., 2007, arXiv:0711.0642 [math.MG].
- [13] McCarthy, D. D., and G. Petit, 2003, *IERS Technical Note No 32*, Technical Report, IERS Convention Centre, URL <http://www.iers.org/iers/publications/tn/tn32/>.
- [14] Moritz, H., 1980, *Bull. Geod.* **54**(3), 395.
- [15] Nefedjev, Y. A., and A. I. Nefedjeva, 2005, *Astron. Nachr.* **326**(8), 773.
- [16] Radau, M. R., 1882, *Ann. l'Observ. Paris, Memoires* **16B**, 1.
- [17] Stone, R. C., 1996, *Publ. Astron. Soc. Pac.* **108**, 1051.
- [18] Syndergaard, S., 1998, *J. Atm. Sol.-Terr. Phys.* **60**(2), 171.
- [19] Yatsenko, A. Y., 1995, *Astron. Astroph. Suppl.* **111**(3), 579.